Preconditioning input data for full waveform inversion using dipole sparse tau-p inversion

Ziqin Yu, Ping Wang, Brad Wray, Suryadeep Ray, Wei Zhao, Zhigang Zhang (CGG)*

Summary

Low-frequency seismic data are crucial for the success of full waveform inversion (FWI) used in velocity model building. Marine acquisition technologies have evolved to increase low-frequency seismic signals. However, significant low-frequency noise, often caused by water flowing across the streamers, still alters the signal-to-noise ratio. We propose to use an algorithm based on a dipole sparse tau-p inversion to attenuate low-frequency and high-dip noise. When applied to synthetic and real data sets, this method provides clean low-frequency input data to enhance the performance of FWI.

Introduction

Full waveform inversion is widely used for building velocity models (Tarantola 1984; Virieux and Operto 2009). With the advancement of hardware and software, and the improvement of algorithmic efficiency, FWI has been successfully applied to 3D real data with different acquisition patterns (Plessix 2009; Sirgue et al. 2010; Vinje et al. 2012; Ratcliffe et al. 2013; Jones et al. 2013; Mothi et al. 2013).

Low-frequency seismic data with a good signal-to-noise ratio (S/N) are crucial for the success of FWI. A case study by Baeten (2013) has shown that FWI starting from 1.5 Hz leads to a successful update of velocity while starting from 2 Hz fails.

Various broadband marine solutions have been proposed to increase the low-frequency seismic signals, and acquisition technologies have evolved to reduce the noise caused by tugging, birds and electrical devices. However, remaining significant low-frequency noise, mostly caused by water flowing across the streamers, impairs the S/N of low-frequency data, which creates challenges for FWI.

Figure 1a shows four input shot gathers before noise attenuation. Figure 1c is the output after standard noise attenuation using f-x projection filtering (Soubaras, 1995). We observed that the standard method did a reasonable job to remove most of the swell noise. However, when we applied a low-pass filter at 4.5 Hz to this output, we noticed that there was still significant low-frequency residual noise which poses a great challenge for FWI (Figure 1d). We also applied the dipole sparse tau-p noise attenuation method proposed by Ray et al. (2014) to the same input data and the output is shown in Figure 1e. While the full-bandwidth results using both denoise attenuation methods look similar (Figures 1c and 1e), the low-frequency (<4.5 Hz) output using the dipole sparse tau-p noise attenuation method (Figure 1f) is significantly cleaner than that using the standard noise attenuation method (Figure 1d). The higher low-frequency S/N provided by the former method is very important for the success of FWI.

Ray et al. (2014) described the mathematical details of the dipole sparse tau-p inversion and attributed the success of their method for low-frequency/high-dip noise attenuation to two factors: (1) the sparse tau-p inversion reduces the energy leakage among different p values and thus gives an more accurate tau-p representation of the input data compared to regular tau-p transform and (2) the dipole term tends to emphasize the high-frequency and low-dip events and thus effectively attenuates low-frequency and high-dip noise while preserving the primaries.

Using both synthetic and field data, we demonstrate that the improved low-frequency S/N due to the dipole sparse tau-p inversion noise attenuation makes FWI more stable, converge faster and the resulting FWI velocity model gives better migration images.

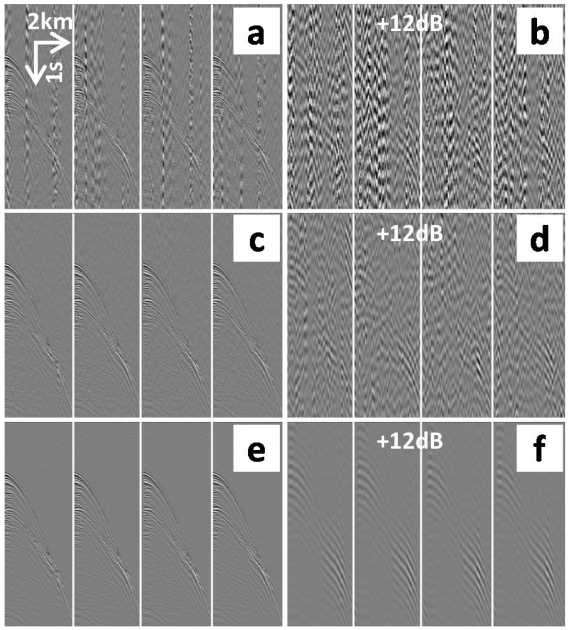

Figure 1: Shot gathers (a) before noise attenuation, (c) after standard noise attenuation, and (e) after noise attenuation using dipole sparse tau-p inversion. Low-pass filtered shot gathers at 4.5 Hz (b) before noise attenuation, (d) after standard noise attenuation, and (f) after noise attenuation using dipole sparse tau-p inversion.

DOI http://dx.doi.org/10.1190/segam2015-5899888.1

Synthetic data example

We tested this dipole sparse tau-p noise attenuation method for FWI data preconditioning on a 2D synthetic data set modeled from an isotropic elastic model provided by Chevron in 2014 for FWI benchmark testing.

This data set contains low-frequency noise to mimic the real world seismic data (Figures 2a and 2b). After dipole sparse tau-p noise attenuation, a clear uplift was observed in the low-frequency panel (Figures 2c and 2d). The raw data had a poor S/N below 3 Hz, which was greatly improved by dipole sparse tau-p noise attenuation (Figure 2d). Next, we evaluated the impact of the improved low-frequency S/N on FWI results.

We used the 1D velocity model provided by Chevron (Figures 3a and 3b) as a starting point for all of our FWI tests. Figures 3c and 3e show the FWI results to 3 Hz and to 10 Hz using the raw data as input, while Figures 3d and 3f show the FWI results to 3 Hz and to 10 Hz using the denoised data as input. The FWI results using the denoised data had fewer swing artifacts (blue circles) and a stronger velocity update (red circles). Compared to the migrated common image gathers (CIGs) using the FWI velocity obtained from the raw data (Figures 3g and 3i), the migrated CIGs using the FWI velocity generated by the denoised data (Figures 3h and 3j) were flatter and better focused, which further validated the denoise approach.

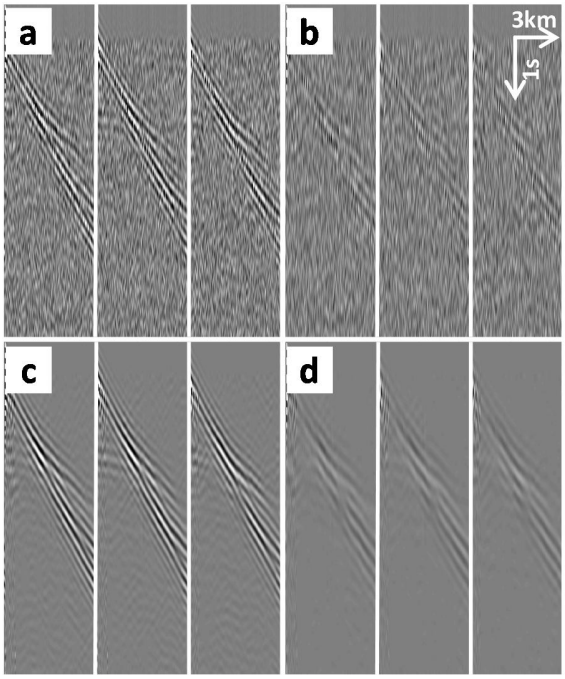

Figure 2: Raw input shot gathers low-pass filtered at: (a) 3.5 Hz and (b) 2.5 Hz. Shot gathers after noise attenuation using dipole sparse tau-p inversion low-pass filtered at: (c) 3.5 Hz and (d) 2.5 Hz.

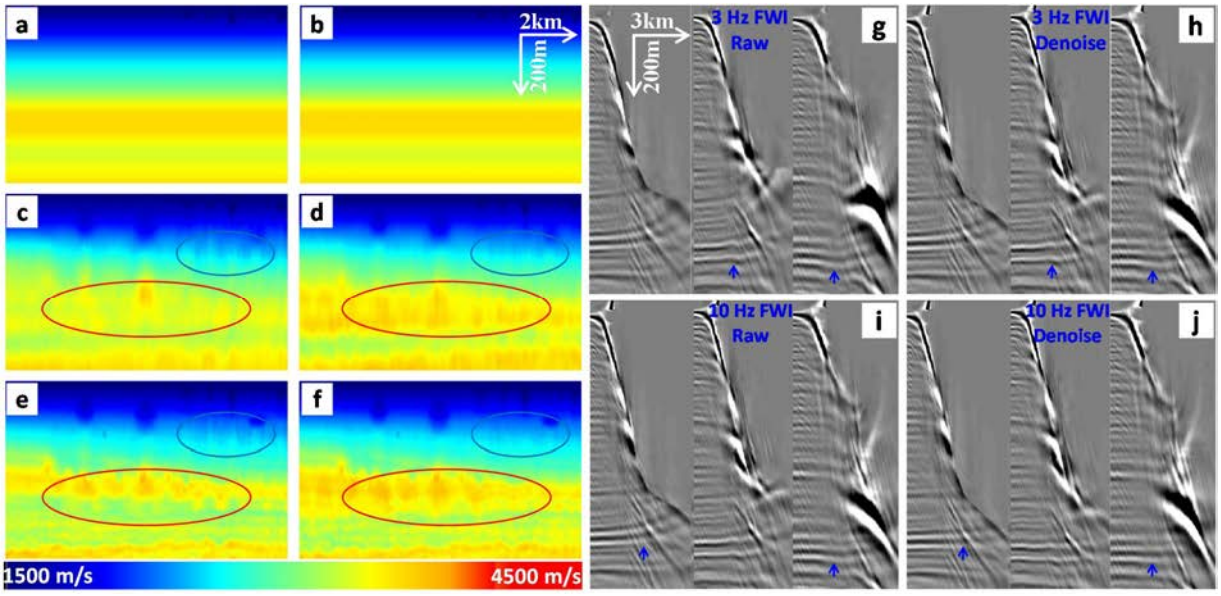

Figure 3: (a) and (b) initial velocity model provided by Chevron. FWI velocity model to: (c) 3 Hz and (e) 10 Hz using the raw input data. FWI velocity model to: (d) 3 Hz and (f) 10 Hz using the denoised input data. Common image gathers (CIGs) migrated with (g) 3 Hz and (i) 10 Hz FWI velocity generated using raw data. CIGs migrated with (h) 3 Hz and (j) 10 Hz FWI velocity generated using denoised data.

DOI http://dx.doi.org/10.1190/segam2015-5899888.1

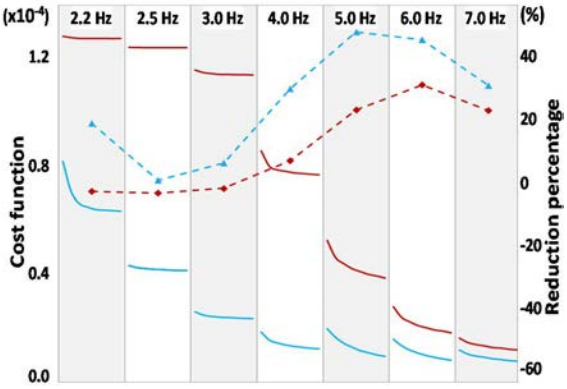

Figure 4: Red and blue solid lines represent the cost function after each iteration using the raw and the denoised input data, respectively. Red and blue dashed lines represent the percentage reduction in the cost function after eight iterations in each frequency range using the raw and the denoised input data, respectively.

Figure 4 compares the absolute value of the cost function (solid lines) and the percentage of its reduction (dashed lines) for each iteration and each frequency. The denoised data resulted in a smaller absolute value of the FWI cost function (solid blue lines) and faster convergence (dashed blue line).

Field data example

The data set was acquired in the deep water Kwanza Basin offshore Angola using a narrow-azimuth, variable-depth, towed-streamer configuration with 8 km maximum offset. The streamer depth varies from 8 m at the nearest offset to 50 m at the furthest offset.

The variable-depth tow data is characterized by a broader bandwidth and an increased S/N at low frequencies due to a larger average receiver depth, particularly at far offsets where the deepest penetrating diving waves are recorded at a receiver depth close to 50 m. The low-frequency S/N after a standard denoise workflow (i.e., swell noise and seismic interference attenuation) is relatively high due to deep receiver depths (Figures 5a-c). Wray et al. (2014) demonstrated that FWI works well for this data set even with a standard denoise workflow (Figures 6a and 6c).

However, there still exists apparent low-frequency and high-dip noise that may adversely affect FWI. After dipole sparse tau-p noise attenuation, we observed better low-frequency signals, in particular below 2.5 Hz (Figure 5f); this provides FWI with a superior input. Next, we checked if this input could give even better FWI results than those obtained by Wray et al. (2014).

For FWI testing, our starting V_0 model comes from high-resolution, ray-based tomography (Guillaume et al. 2011), and the starting ε and δ models come from ray-based tomography with well control applied. Figure 6a shows the FWI-updated velocity to 7 Hz using input data after standard denoise and the migrated CIGs are shown in Figure 6c (Wray et al. 2014). We could observe that this FWI-updated velocity properly flattens most events. The FWI-updated velocity to 7 Hz (Figure 6b) using input data after dipole sparse tau-p inversion looks similar to that in Figure 6a. However, a careful examination reveals that the former has better resolution and better matches the geological features. The migrated CIGs (Figure 6d) using the velocity in Figure 6b are generally flatter and better focused than those (Figure 6c) generated using the velocity in Figure 6a. It is worth re-iterating that FWI using input data after dipole sparse tau-p noise attenuation converges much faster due to a higher low-frequency S/N.

Conclusions and discussion

We showed that the dipole sparse tau-p inversion method effectively attenuates low-frequency and high-dip noise for both synthetic and field data. An improved low-frequency S/N makes FWI more stable, converge faster and the resulting FWI velocity model gives better migration images.

We demonstrated that low-frequency seismic data with a good S/N are crucial for the success of FWI. While various algorithms can be used to attenuate the noise in the acquired seismic data and hence improve the low-frequency S/N for FWI, a more fundamental way to improve the low-frequency S/N is to increase low-frequency seismic signals and reduce low-frequency noise through innovations of marine survey technologies.

Acknowledgements

We thank CGG for permission to publish this work and Chevron and the SEG for providing the 2D 2014 FWI benchmark data set. Special thanks go to Nicolas Chazalnoel for support and discussions.

DOI http://dx.doi.org/10.1190/segam2015-5899888.1

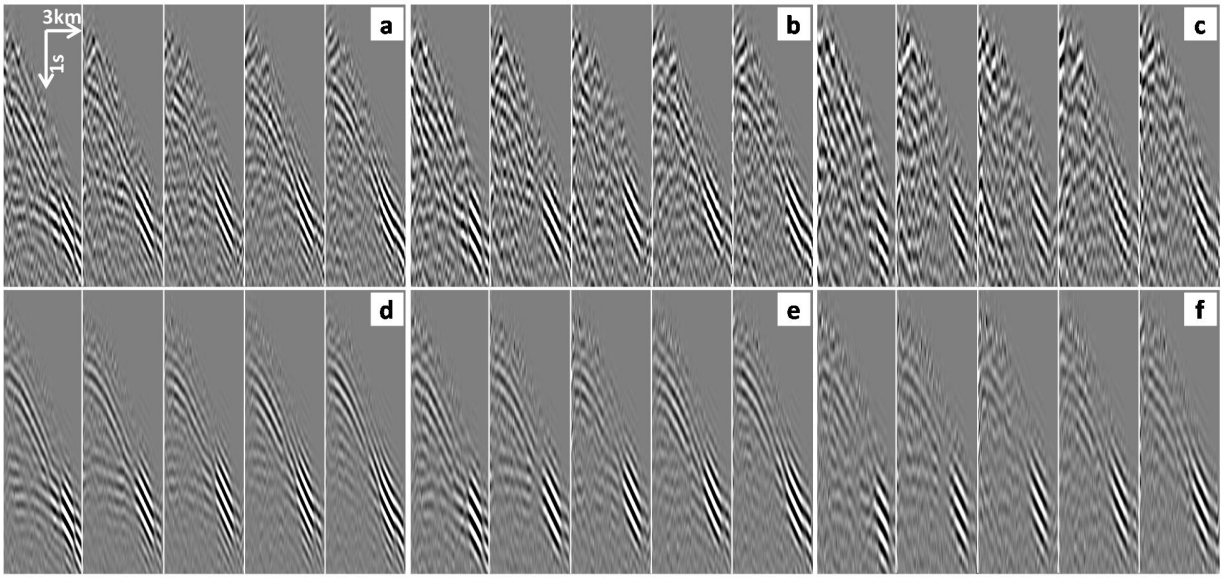

Figure 5: Shot gathers after standard noise removal processing followed by low-pass filters at: (a) 3.5 Hz, (b) 3.0 Hz, and (c) 2.5 Hz. Shot gathers after further noise attenuation using dipole sparse tau-p inversion followed by low-pass filters at: (d) 3.5 Hz, (e) 3.0 Hz, and (f) 2.5 Hz.

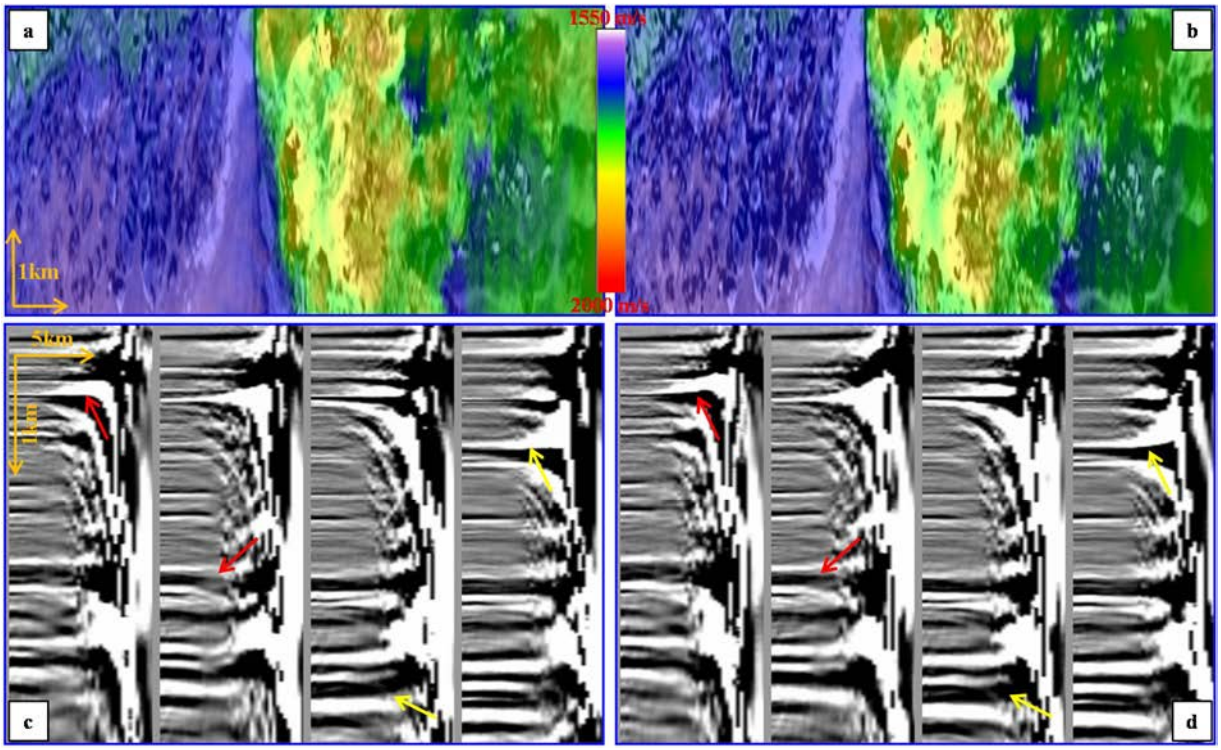

Figure 6: Velocity model updated with FWI using input data after standard denoise workflow: (a) without, and (b) with dipole sparse tau-p inversion denoise. An example of migrated CIGs using: (c) velocity in (a), and (d) velocity in (b), respectively.

DOI http://dx.doi.org/10.1190/segam2015-5899888.1

EDITED REFERENCES

Note: This reference list is a copyedited version of the reference list submitted by the author. Reference lists for the 2015 SEG Technical Program Expanded Abstracts have been copyedited so that references provided with the online metadata for each paper will achieve a high degree of linking to cited sources that appear on the Web.

REFERENCES

Baeten, G., J. W. de Maag, R.-E. Plessix, R. Klaassen, T. Qureshi, M. Kleemeyer, F. Kroode, and Z. Rujie, 2013, The use of low frequencies in a full-waveform inversion and impedance inversion land seismic case study: Geophysical Prospecting, **61**, no. 4, 701–711. http://dx.doi.org/10.1111/1365-2478.12010.

Guillaume, P., G. Lambaré, S. Sioni, D. Carotti, P. Depre, G. Culianez, J. P. Montel, P. Mitouard, S. Depagne, S. Frehers, and H. Vosberg, 2011, Geologically consistent velocities obtained by high definition tomography: 81st Annual International Meeting, SEG, Expanded Abstracts, 4061–4065.

Jones, C., M. Evans, A. Ratcliffe, G. Conroy, R. Jupp, J. Selvage, and L. Ramsey, 2013, Full-waveform inversion in a complex geological setting: a narrow azimuth towed streamer case study from the Barents Sea: 75th Annual International Conference and Exhibition, EAGE, Extended Abstracts, http://dx.doi.org/10.3997/2214-4609.20130830.

Mothi, S., K. Schwarz, and H. Zhu, 2013, Impact of full-azimuth and long-offset acquisition on full-waveform inversion in deep water Gulf of Mexico: 75th Annual International Conference and Exhibition, EAGE, Extended Abstracts, http://dx.doi.org/10.3997/2214-4609.20130826.

Plessix, R. E., 2009, Three-dimensional frequency-domain full-waveform inversion with an iterative solver: Geophysics, **74**, no. 6, WCC149–WCC157. http://dx.doi.org/10.1190/1.3211198.

Ratcliffe, A., R. Jupp, R. Wombell, G. Body, V. Durussel, A. Fernandes, B. Gosling, and M. Lombardi, 2013, Full-waveform inversion of variable-depth streamer data: An application to shallow channel modeling in the North Sea: The Leading Edge, **32**, 1110–1115. http://dx.doi.org/10.1190/tle32091110.1.

Ray, S., Z. Zhang, Z. Fu, L. Liu, and P. Wang, 2014, Noise attenuation using a dipole sparse Tau-P inversion: 84th Annual International Meeting, SEG, Expanded Abstracts, 4213–4217. http://dx.doi.org/10.1190/segam2014-1194.1.

Sirgue, L., O. I. Barkved, J. Dellinger, J. Etgen, U. Albertin, and J. H. Kommedal, 2010, Full-waveform inversion: The next leap forward in imaging at Valhall: First Break, **28**, no. 4, 65–70.

Soubaras, R., 1995, Prestack random and impulsive noise attenuation by f-x projection filtering: 65th Annual International Meeting, SEG, Expanded Abstracts, 525–527.

Tarantola, A., 1984, Inversion of seismic reflection data in acoustic approximation: Geophysics, **49**, 1259–1266. http://dx.doi.org/10.1190/1.1441754.

Vinje, V., A. Ratcliffe, A. Bertrand, T. Hellmann, and Y. Belhassen, 2012, Improved PP- and PS-imaging using full-waveform inversion — Tommeliten OBC case study: 74th Annual International Conference and Exhibition, EAGE, Extended Abstracts, W010.

Virieux, J., and S. Operto, 2009, An overview of full-waveform inversion in exploration geophysics: Geophysics, **74**, no. 6, WCC1–WCC26. http://dx.doi.org/10.1190/1.3238367.

Wray, B., N. Chazalnoel, W. Zhao, and H. Zhu, 2014, Full-waveform inversion using broadband variable-depth streamer data in deep water West Africa: 76th Annual International Conference and Exhibition, EAGE, Extended Abstracts, http://dx.doi.org/10.3997/2214-4609.20147413.

DOI http://dx.doi.org/10.1190/segam2015-5899888.1